Interferometric synthetic aperture radar observations of the 1994 Double Spring Flat, Nevada, earthquake (M5.9): Main shock accompanied by triggered slip on a conjugate fault

Falk Amelung[1]

Rosenstiel School of Marine and Atmospheric Sciences, University of Miami, Florida, USA

John W. Bell

Nevada Bureau of Mines and Geology, University of Nevada, Reno, Nevada, USA

[1] The 1994 Double Spring Flat (DSF) earthquake (M5.9) was the largest earthquake to strike Nevada in more than 30 years. It occurred in the Sierra Nevada-Basin and Range Transition Zone within a step-over region between two major normal faults. Descending and ascending ERS interferograms show a maximum range change of 8.5 cm which is the coseismic ground displacement associated with this normal, oblique-slip, moderate-sized earthquake. Elastic inverse modeling and surface displacements across coseismic ground cracks suggest that two different event sources could account for the observed deformation. The first source was the main shock with right-oblique slip on the north-northwest striking DSF fault. The second source was normal faulting on a shallow, north-northeast striking, elongated plane (conjugate to the DSF fault). These two sources are consistent with the pattern of postevent seismicity, and we suggest that the second source represents seismic and aseismic slip triggered by the main shock. Calculations of changes in Coulomb failure stress show that the main shock encouraged normal slip on this plane. *INDEX TERMS:* 1206 Geodesy and Gravity: Crustal movements—interplate (8155); 1241 Geodesy and Gravity: Satellite orbits; 1242 Geodesy and Gravity: Seismic deformations (7205); 1299 Geodesy and Gravity: General or miscellaneous; 7212 Seismology: Earthquake ground motions and engineering; *KEYWORDS:* earthquake, InSAR, Nevada, interferogram, conjugate, trigger

1. Introduction

[2] The western Basin and Range province at the latitude of $38°-41°$N is among the tectonically most active areas in North America. Recent GPS studies show that the Sierra Nevada Block moves $10-12$ mm/yr toward north-northwest with respect to the central Basin and Range province and the stable continental interior [e.g., *Bennett et al.*, 1999]. The western Basin and Range region accounts for 25% of the relative motion between the North American and the Pacific plates.

[3] The western Basin and Range province has been the location of six magnitude 7 or greater earthquakes since 1850 [*dePolo and dePolo*, 1998]. The 1915 M7.8 Pleasant Valley earthquake (Figure 1a) is among the largest historic normal faulting earthquakes recorded in the western United States. The 1954, M7.2 Fairview peak earthquake was part of a 6-month sequence of four $M > 6.6$ earthquakes which is one of the world's best examples for earthquake interaction [*Hodgkinson et al.*, 1996; *Caskey et al.*, 1996]. Smaller western Basin and Range earthquakes may display unusual features. The 1950 Ft Sage earthquake (50 km north of Reno) was only M5.6 but had about 15 cm of vertical surface rupture [*Gianella*, 1957].

[4] The M5.9 Double Spring Flat (DSF) earthquake of 12 September was the largest earthquake to struck Nevada during the past 30 years. The earthquake was accompanied by ground cracking and was followed by a complex aftershock sequence. In this paper we utilize interferometric synthetic aperture radar (InSAR) to examine possible dislocation models for the event and together with ground rupture and aftershock patterns to develop a preferred source mechanism.
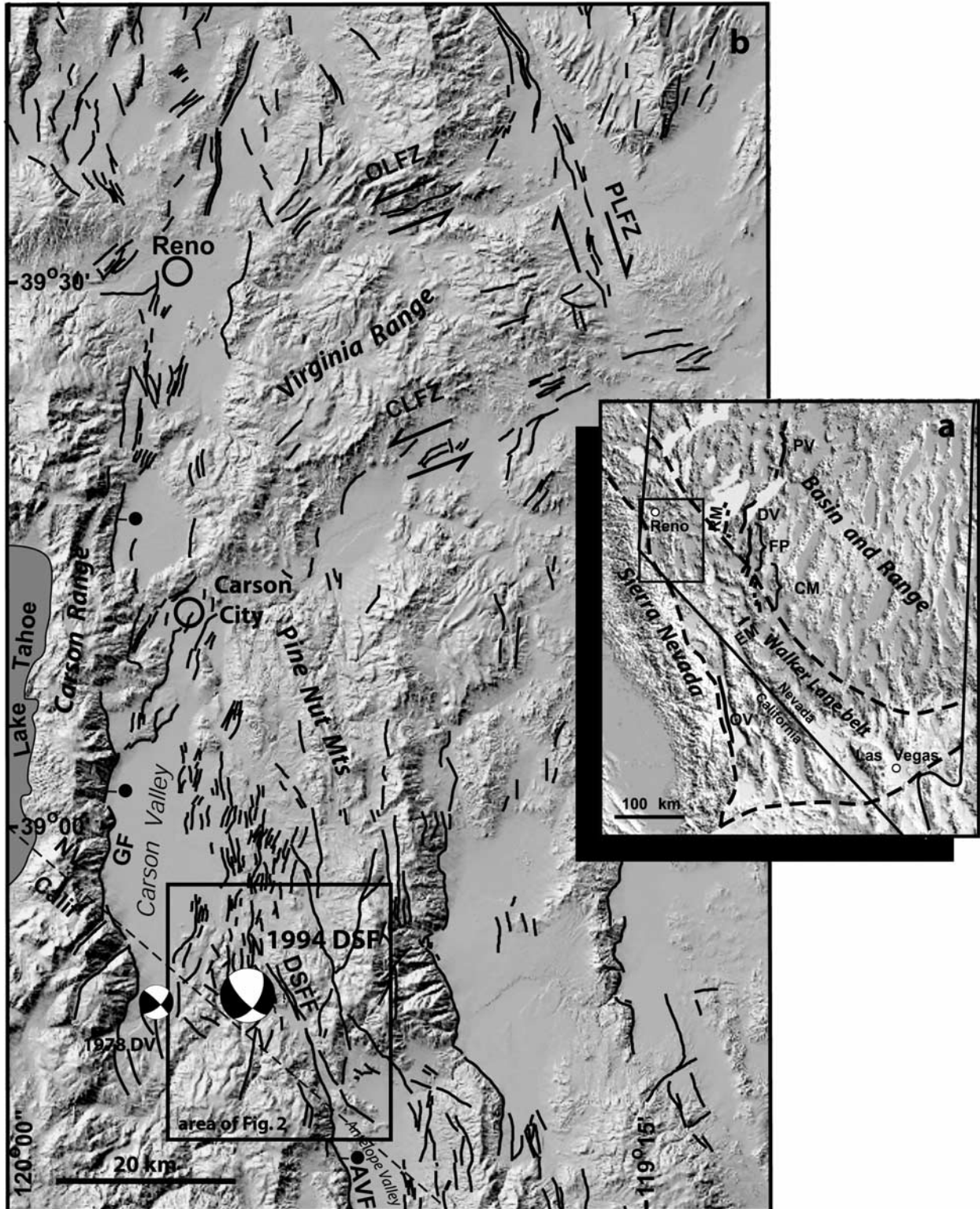
2. Tectonic Setting

[5] The epicentral area of the DSF earthquake (Figure 1b) is located 30 km south of Carson City within a complex network of generally north trending late Quaternary faults in

---

[1]Formerly at Hawaii Institute of Geophysics and Planetology, School of Ocean and Earth Science and Technology, University of Hawaii at Manoa, Honolulu, Hawaii, USA.

the Basin and Range-Sierra Nevada transition zone (SNTZ). The region is part of the Walker Lane belt (WLB), a broad zone of strike-slip and normal faulting extending along a 700-km-long zone in western Nevada (Figure 1a). Right-lateral shear along northwest striking faults accounts for as much as 48–75 km of cumulative motion across the WLB in the last 25–30 Myr [*Stewart*, 1988]. This long-term motion is consistent with the broad pattern of contemporary northwest directed shear observed by geodesy [*Bennett et al.*, 1999; *Thatcher et al.*, 1999; *Wernicke et al.*, 2000; *Oldow et al.*, 2001; *Svarc et al.*, 2002].

[6] The historically most active portion of the western Basin and Range region is the central Nevada seismic belt (CNSB), a 300-km-long zone of historical *M*6.6–7.6 earth-

quakes and nearly continuous surface faulting. The CNSB extends north from the central portion of the WLB. This zone includes the 1915 Pleasant Valley earthquake (M7.8), the 1932 Cedar Mountain earthquake (M7.2) [*Bell et al.,* 1999], the 1934 Excelsior Mountain earthquake (M6.3), the 1954 Rainbow Mountain-Stillwater earthquakes (M6.6 and M6.8), and the 1954 Fairview Peak and Dixie Valley earthquakes (M7.1 and M6.8) (Figure 1a, magnitudes from *dePolo and dePolo* [1998]).

[7] The principal faults in the SNTZ include the right-lateral Pyramid Lake fault zone, and conjugate left-lateral fault zones, the Olinghouse and Carson lineaments (Figure 1b). Normal faulting kinematically associated with the strike-slip motion of the region may be related to slip partitioning [*Wesnousky and Jones,* 1994] or temporal variations in the stress field [*Zoback,* 1989]. The Genoa fault (GF) is the largest of the regional normal faults; it is the range-bounding fault of the Carson Range, marking the principal boundary of the SNTZ. The fault has not ruptured historically, but it has a geologic slip rate of $\geq 1 - 2$ mm/yr, the highest presently known slip rate for any fault in the western Basin and Range province [*Ramelli et al.,* 1999]. On the basis of geodesy, as much as 6 mm/yr of contemporary strain may be accommodated by the SNTZ in the vicinity of Carson City [*Thatcher et al.,* 1999]. The Antelope Valley fault (AVF), is a similar range-bounding normal fault of the SNTZ with an estimated geologic slip rate of ~ 0.7 mm/yr [*dePolo and Anderson,* 2000]. Differential motion determined from GPS between Antelope Valley and the Sierra Nevada block is between 3 and 7 mm/yr [*Oldow et al.,* 2001].

[8] The DSF earthquake occurred in the structural left step-over region between the Genoa and Antelope Valley faults, an area characterized by northwest to north striking faults (Figure 1b). The principal fault in this area is the northwest striking, southwest dipping Double Spring Flat fault (DSFF) which links a series of right- and normal-oblique-slip faults along the western margin of the Pine Nut Mountains to the northwest with the Antelope Valley fault in the southeast. These faults exhibit scarps in young alluvium and thus are of Quaternary age, but slip rates are not presently known. A M5.0 earthquake occurred along similar faults in Diamond Valley 10 km to the west of Double Spring Flat in 1978 [*Somerville et al.,* 1980].

3. The 1994 Double Spring Flat Earthquake Sequence

[9] The Double Spring Flat earthquake occurred on 12 September 1994 at 0523 LT (Pacific Standard Time). This earthquake was widely felt in the Reno-Carson City region and had a moment magnitude of $M_w5.85$ [*Ichinose,* 2000] (for simplicity, we round the magnitude to M5.9). The earthquake caused only little damage because the epicentral area was not inhabited. The main shock was a normal, oblique-slip event with the epicenter placed about 3 km west of the DSF fault at a focal depth of 6 km [*Ichinose et al.,* 1998].

[10] The main shock was followed by an energetic aftershock sequence [*Ichinose et al.,* 1998]. The largest aftershock was a $M_w5.3$ normal event and occurred 12 hours after the main shock ~ 5 km southeast of the main event (Figure 2). We refer to this event as the principal aftershock. The aftershocks occurred along two principal conjugate trends: the first days of aftershocks occurred primarily along north-northeast alignments and later aftershocks occurred along north-northwest alignments (Figure 2a). Most of the north-northeast trending aftershocks were normal-slip faulting events (Figure 2a), which cannot be associated to any mapped faults. The north-northwest trending after-shocks were right-normal oblique-slip events along the DSF fault with focal mechanisms similar to the main shock. Over two years, aftershocks migrated southward onto another sets of conjugate faults and then onto the Antelope Valley fault zone [*Ichinose et al.,* 1998]. The aftershock sequence included 16 $M > 4$ aftershocks, most of them located along the DSF fault. The main shock was accompanied by minor ground cracking of $1 - 20$ mm along several of the north-northwest trending faults (Figure 2) [*Ramelli et al.,* 1994].

[11] On the basis of the pattern of foreshocks and after-shocks, *Ichinose et al.* [1998] concluded that the main event was a left-lateral oblique-slip event on the north-northeast trending nodal plane. In contrast, in this paper we will argue that the main shock instead ruptured the north-northwest trending nodal plane, and that it had right-lateral strike-slip motion. Throughout this paper the earthquake data of *Ichinose* [2000] are used which supercede that of *Ichinose et al.* [1998] and include the $M_w5.3$ aftershock not included in the original data set (G. Ichinose, personal communication, 2001).

4. InSAR Data

[12] To examine the ground displacements associated with this earthquake sequence, we produced interferograms using SAR data acquired by the European ERS-1 and ERS-2 satellites (C-band radar, wavelength 5.6 cm). These are the only geodetic data available for this earthquake

---

Figure 1. (opposite) (a) Location map of the Sierra Nevada-Basin and Range transition zone showing the study area (inset box) and historical earthquake rupture zones associated with the central Nevada seismic belt: 1872 Owens Valley (OV), 1915 Pleasant Valley (PV), 1932 Cedar Mountain (CM), 1934 Excelsior Mountain (EM), 1954 Rainbow Mountain-Stillwater (RM), 1954 Fairview Peak (FP) and 1954 Dixie Valley (DV). Dashed line outlines the Walker Lane belt. (b) Map showing location of the Double Spring Flat (DSF) main event and principal structural tectonic features of the western Nevada region. The earthquake occurred in a broad transition zone between the Sierra Nevada and Basin and Range province; principal regional faults include the right-lateral strike-slip Pyramid Lake fault zone (PLFZ), the left-lateral strike-slip Olinghouse (OLFZ) and Carson Lineament (CLFZ) fault zones, and the normal Genoa (GF) and Antelope Valley (AVF) faults. Normal faults are marked by solid circles. The earthquake occurred along the Double Spring Flat fault (DSFF) which forms part of a complex structural step over between the GF and AVF zones. The focal mechanisms for the DSF main shock and for the 1978 M5 Diamond Valley event (DV) are also shown.
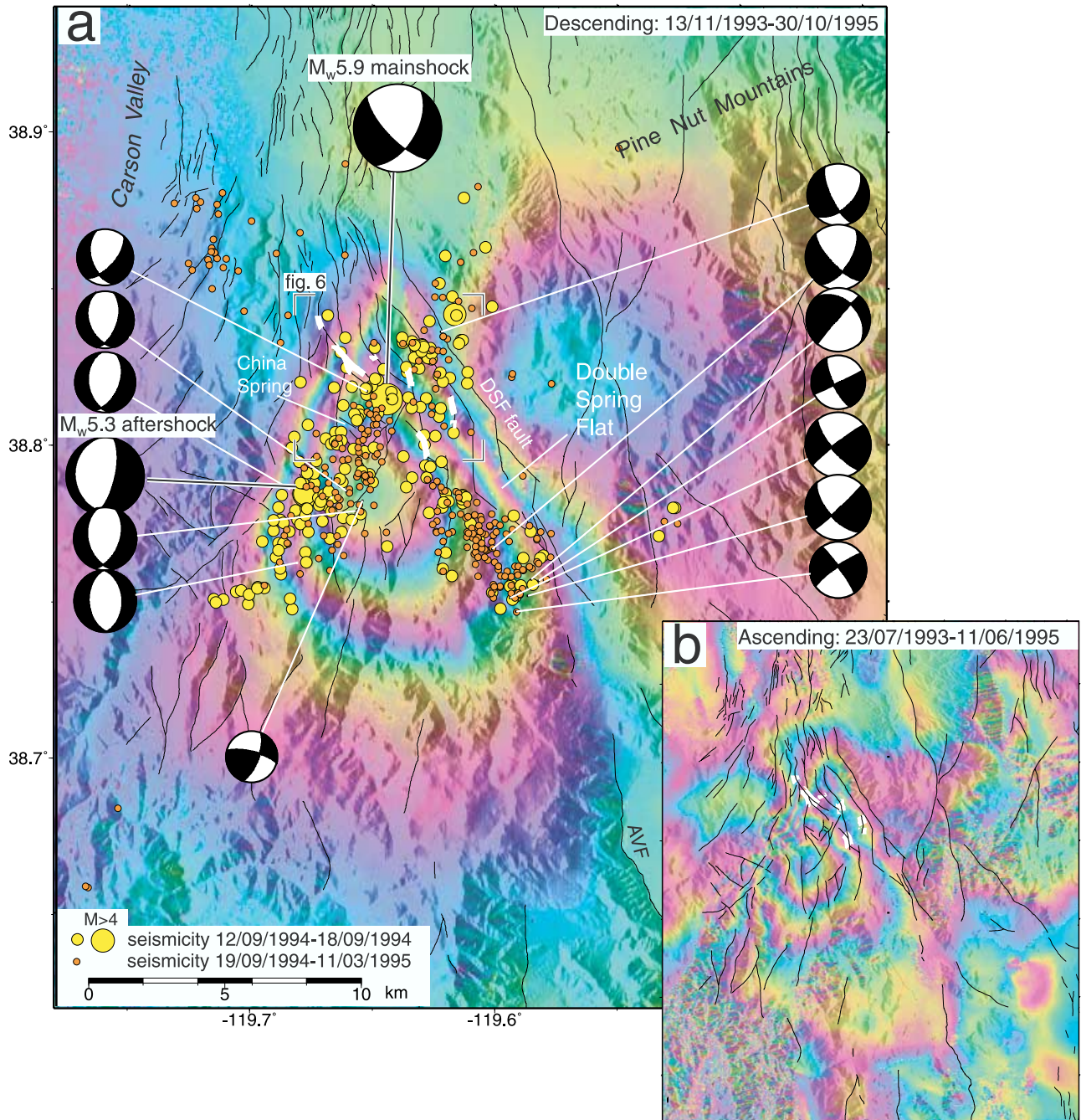
Figure 2. Ground deformation, aftershock locations and focal mechanisms of largest events associated with the DSF earthquake sequence. Wrapped phase of (a) descending and (b) ascending 1993–1995 interferograms. One color cycle represents 2.8 cm range displacement. The aftershocks follow two conjugate trends with the first week of aftershocks (yellow) primarily along north-northeast. Coseismic ground cracks are shown by white lines. Aftershock locations and waveform-derived focal mechanisms are from *Ichinose* [2000].

sequence. The closest GPS campaign station is located at ~20 km from the epicenter [*Oldow et al.*, 2001] where coseismic ground deformation is negligible.

[13] We formed a descending interferogram using 30 November 1993 and 19 October 1995 images (radar looking west, Figure 2a) and an ascending interferogram using 23 July 1993 and 11 June 1995 images (radar looking east, Figure 2b). The perpendicular baseline separation between the satellite orbits is ~7 m for the descending and ~160 m for the ascending interferogram. We removed the topographic phase using a 30 m USGS digital elevation model so that the phase in the interferogram represents ground displacements in radar line-of-sight (LOS) direction. One cycle of phase difference corresponds to 2.8 cm LOS displacement. The unit vector in LOS direction in an East, North, Up coordinate system is −0.34, 0.08, −0.94 for the

descending interferogram and 0.29, 0.07, −0.95 for the ascending interferogram. This shows that the ERS radar is most sensitive to vertical displacements and least sensitive to north-south displacements. East-west oriented displacements will cause LOS displacement with opposite sign in descending and ascending interferograms.

[14] The interferometric phase in the descending interferogram (Figure 2a) is clear and undisturbed, further illustrating that dry environmental conditions in Nevada are very favorable for InSAR measurements [*Amelung et al.*, 1999]. The ascending interferogram, however, shows atmospheric effects of up to 1 phase cycle. Processing of additional interferograms showed that the atmospheric effects originate from the 23 July 1993 image which is the only preearthquake image available for this orbit.

[15] The main phase feature in both the descending and ascending interferograms is a teardrop-shaped area of up to 8.5 cm of range increase (three color fringes) located between the west margin of the north-northwest trending aftershock zone and the DSF fault. This feature is characterized by a triangle-shaped phase pattern in the north, and a linear area of relatively high range change gradient in the west. We refer to this feature as the teardrop feature. The similar shape of the teardrop feature in both interferograms indicates that the ground displacement is vertical subsidence. The descending interferogram also shows an area of up to 2.5 cm of range decrease (uplift) east of the teardrop feature (∼0.8 fringe, yellow-red-blue-green colors). The ascending interferogram also shows an area of up to 2.8 cm of range decrease west of the teardrop feature (1 fringe, red-blue-green colors).

[16] The precise timing of the ground deformation can not be determined from the InSAR data being constrained only by the dates of the November 1993 and October 1995 images. We also obtained interferograms for 1995–1998 but did not find evidence of any postseismic deformation during this period. Throughout this paper we assume that ground deformation occurred during the main DSF earthquake sequence.

5. Elastic Modeling

[17] We use elastic dislocation modeling to constrain the source mechanism of the main earthquake sequence, based on the solutions for uniform dislocations in an elastic half-space [*Okada*, 1992]. Instead of modeling the phase at each pixel in the interferogram we reduce the amount of data using a quadtree decomposition algorithm. In this procedure the phase-unwrapped interferogram is divided into four equal sized quadrants and for each quadrant the mean and the root-mean-square deviation of the phase is calculated. If for a given quadrant the root-mean-square deviation is below a given threshold value, the mean of the phase is retained as a data point. If the root-mean-square deviation is above the threshold value, this quadrant is again divided into four quadrants. This procedure is repeated until the interferogram is divided into many different sized squares each with root-mean-square deviation below the threshold value. The modeled data set consists of the mean of the phase in each square. The advantage of quadtree decomposition is that it leaves many data points in areas of high LOS displacement gradients but only few data points in areas of

no or little LOS displacement gradients. The algorithm is explained in more detail by *Jonsson et al.* [2002].

[18] The threshold values chosen need to be above the variance of the atmospheric phase effects. Using thresholds of 3.5 mm for the descending interferogram and of 7.0 mm for the ascending interferograms we obtain 713 data points for the descending interferogram and in 289 data points for the ascending interferogram. The phase-unwrapped interferograms together with the quadtree decompositions are shown in Figure 3. We have removed data points related to the high LOS displacement gradients near the ground cracks which we do not attempt to model.

[19] Best fitting models are characterized by a minimum of the misfit function $\mathrm{sqrt}(1/N \, \Sigma_i (d_i - m_i)^2)$ between observed displacements d_i and model predictions m_i (normalized root-mean-square, RMS). N is the number of data points. The descending interferogram contributes 71% and the ascending interferogram 29% to the misfit function, somewhat reflecting the different degree of atmospheric noise in the interferogram. We use a Monte Carlo-type simulated annealing algorithm [*Cervelli et al.*, 2001] to solve this nonlinear inverse problem. This algorithm usually escapes local minima and finds the global minimum of the misfit function [*Cervelli et al.*, 2001, 2002; *Jonsson et al.*, 2002].

[20] Our definition of the misfit function implies the assumption that the errors of the InSAR data are uncorrelated. Spatial variations of atmospheric water vapor, however, result in correlated errors of the InSAR data [*Williams et al.*, 1998; *Hanssen*, 2001; *Jonsson*, 2002]. A cold front, for example, can produce signal delays of up to 8 cm [*Hanssen*, 2001]. The simplified treatment of the errors of the data has to be kept in mind when interpreting small differences in misfit as we do below.

5.1. Single Dislocation Model

[21] We first assume that ground deformation was caused by a single, uniform, elastic dislocation and solve for each of the nine parameters describing the dislocation: strike, dip, length and width, three parameters for the location, and two components of the slip vector. The best fitting single dislocation model involves right-normal slip on a north-northwest striking, west dipping plane with 58% of the moment due to strike-slip displacement (model A, Figures 4c and 4d and Table 1). The geometry of this dislocation is consistent with the DSF fault and with the main shock focal mechanism. However, several features of the interferograms are not reproduced by this model, such as the triangle-shaped phase signature at the northern tip of the teardrop feature and the linear, north-northeast trending area of relatively high range change gradient at the west margin of the teardrop feature. This discrepancy between observed and modeled LOS displacements suggests that this earthquake sequence consists of more than one source.

5.2. Double Dislocation Models

[22] We next consider models with two uniform dislocations: one dislocation associated with the main shock and the other dislocation associated with the principal aftershock. To investigate which of the nodal planes ruptured, we consider alternative model configurations with the main shock first on the north-northwest striking plane (nodal
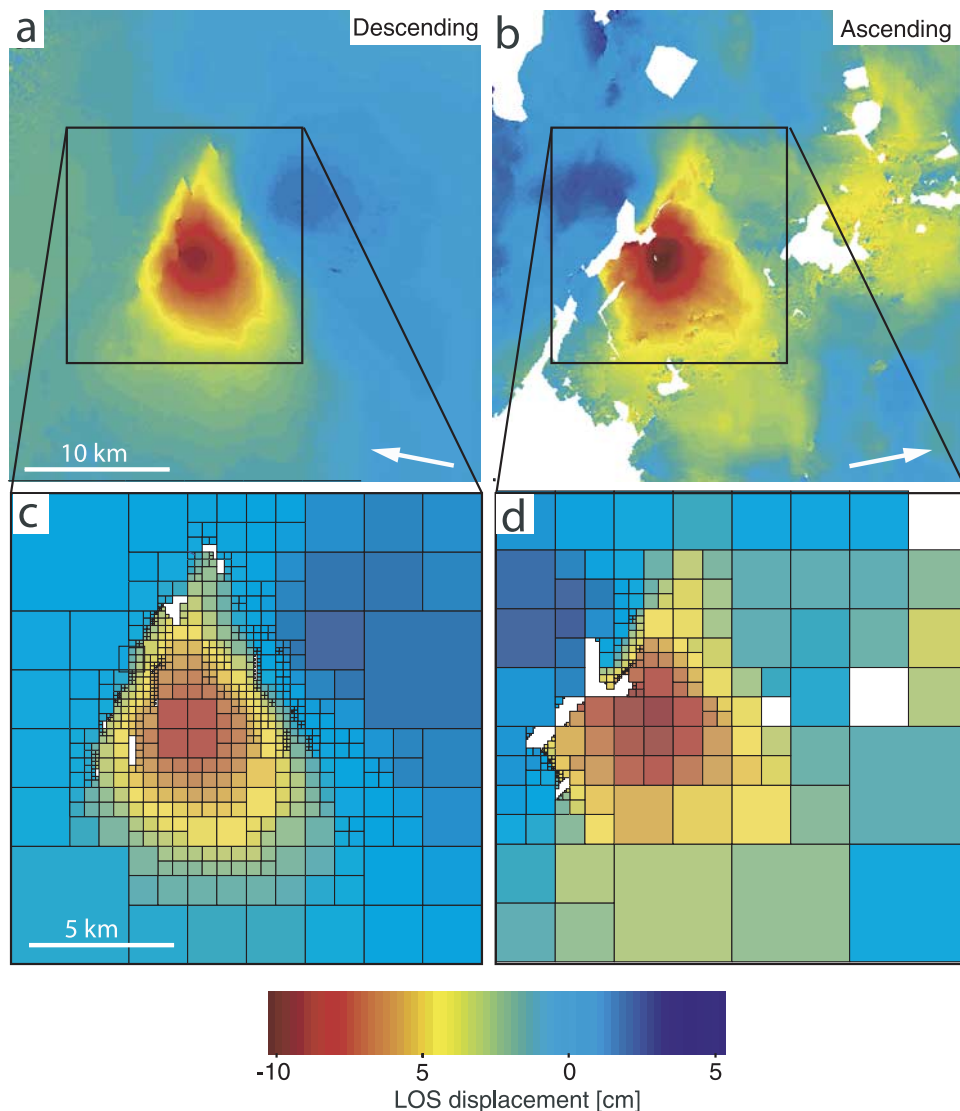
Figure 3. (a) Descending and (b) ascending phase-unwrapped interferograms. (c, d) Central part of quadtree-decomposed interferograms used for elastic modeling. The arrows indicate the radar look direction.

plane 1, the DSF fault) and then on the north-northeast striking nodal plane (nodal plane 2). We assume that the strike, dip and rake of the two dislocations are within ±10° of the seismic moment tensor solution of the main shock and of the principal aftershock (given in Table 1). We also assume that the geodetic moments are equal to, or greater than, the seismic moments but we do not make any assumptions about the dimensions of the dislocation. Using these constraints, we then invert for the 18 fault parameters. Inversions for the parameters of two dislocations without any constraints produced no physically plausible solutions.

[23] The best fitting model for the main shock is on the north-northwest striking nodal plane (model B, Figures 4e and 4f and Table 1). The solution for the alternative model configuration (main shock on the north-northeast striking nodal plane) is characterized by a higher RMS (model C, Figures 4g and 4h, RMS = 5.7 mm versus 5.3 mm for model B). Both models reproduce the teardrop-shaped subsidence area well. The principal weakness of model B

is that it shows too much predicted range decrease west of the teardrop, while the principal weakness of model C is that it shows too much predicted range decrease east of the tear drop. In both model configurations the second dislocation involves a small amount of normal slip (0.16 m) on a shallow, elongated fault (dimensions 2 km by 12 km, Table 1). The inclusion of this dislocation closely reproduces the relatively high range change gradient along the west margin of the teardrop feature in both models. The width-to-length and the slip-to-length aspect ratios of this secondary dislocation are much smaller than typical aspect ratios for moderate earthquakes suggesting that the geodetic moment (M_w5.6) represents mostly aseismic slip.

[24] In order to determine if the modeling results are sensitive to how the data were sampled from the interferograms and to the relative weighting between descending and ascending data, we also carried out inversions using data sets obtained using different values in the quadtree decomposition, by sampling on uniform grids, and by using
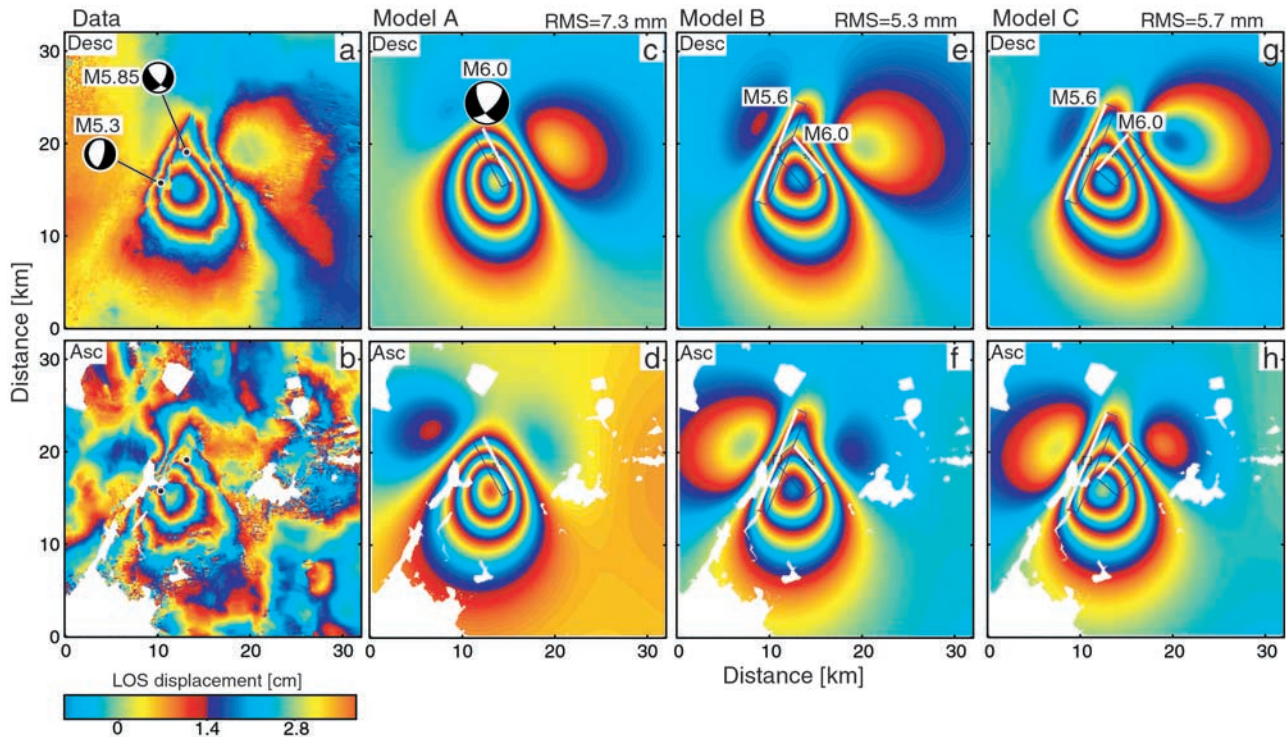
Figure 4. Best fitting elastic dislocation models for the DSF earthquake sequence. (a) Descending and (b) ascending interferograms. (c, d) Single dislocation model, (e, f) double dislocation models with the main event on the north-northwest trending nodal plane, and (g, h) with the main shock on the north-northeast trending nodal plane.

different weighting schemes between the interferograms. In each case the two dislocations of the best fit models were similar to those of model B indicating that these are robust results.

6. Ground Cracks and Surface Faulting

[25] The earthquake was accompanied by minor ground cracks along five of the numerous north-northwest trending faults within a 4 km radius of the epicenter (Figures 2 and 5)

[*Ramelli et al.*, 1994]. The length of the cracks ranged from 0.1 to 2.8 km, and they displayed extensional openings up to 2 cm. The most pronounced crack located northeast of the epicenter showed possible evidence of right-lateral slip (A. Ramelli, personal communication, 2002).

[26] The descending interferogram shows that this crack is associated with a phase discontinuity over a 1.5 km distance at the northern tip of the teardrop feature (Figure 5). This phase discontinuity is clearly related to right-lateral surface displacement along the crack; it cannot

Table 1. Seismic and Geodetic Earthquake Parameters for the Double Spring Flat Earthquake Sequence

M_w[a]	Strike[b]	Dip[b]	Rake[b]	Length,[b] km	Width,[b] km	Slip, m	Depth,[c] km	East,[c] km	North,[c] km	RMS,[d] mm
				Seismic Moment Tensor Solution[e]						
5.85	316	70	142	nodal plane 1	of main shock					
	211	55	25	nodal plane 2						
5.27	193	68	81							
				Model A: Single Dislocation						
5.95	331	62	150	6.6	2.6	1.55	4.8	13.8	18.8	7.3
				Model B: Double Dislocation With Main Shock on Nodal Plane 1						
5.97	319	72	152	5.3	8.5	0.64	3.8	14.3	18.8	5.3
5.51	202	69	88	11.7	3.1	0.16	2.0	10.8	19.3	
				Model C: Double Dislocation With Main Shock on Nodal Plane 2						
5.96	221	59	18	5.2	5.3	1.00	4.3	13.6	19.1	5.7
5.47	203	66	77	11.3	2.9	0.15	2.2	10.7	19.1	

[a]Moment magnitude.
[b]Strike clockwise from north, dip toward right from horizontal, along-strike length and down-dip width.
[c]Center of upper edge of dislocation relative to lower left corner of Figure 2 at UTM (257098E,4280000N).
[d]Normalized root mean square of residuals, sqrt($1/N \Sigma i(di - m_i)^2$) between data and model predictions.
[e]From *Ichinose* [2000]. Nodal plane 1 refers to the north-northwest striking DSF fault and nodal plane 2 to the north-northeast striking trend.
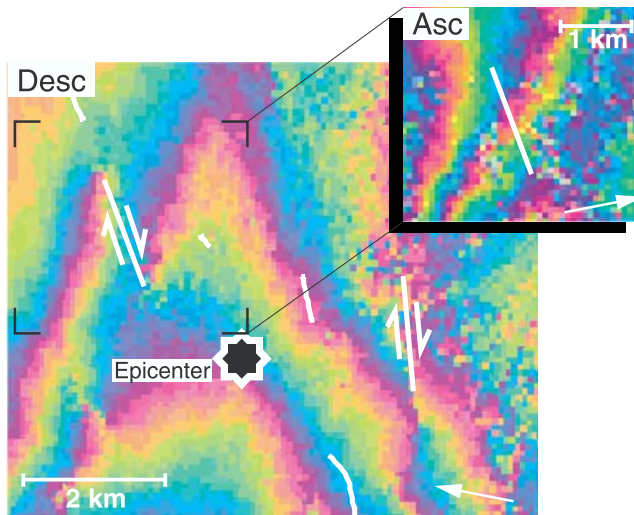
Figure 5. Descending interferogram of the epicentral area showing ground deformation associated with the ground cracks (indicated by white lines). Inset shows the ascending interferogram for the area of the most pronounced crack. The interferograms and ground cracks are displayed in radar coordinates.

be caused by vertical displacements because the ascending interferogram lacks a similar phase discontinuity. The ascending interferogram is not sensitive to along-crack horizontal displacements because the radar looks nearly perpendicular to the crack so that any motion shown would be vertical. The ground displacements extend up to 1 km from the mapped crack, indicating that this is crustal deformation and not a local effect. Note that the easternmost crack is also associated with a right-lateral phase discontinuity (Figure 5) but this feature is more difficult to interpret because of low coherence.

7. Triggered Slip on a Conjugate Fault

[27] The results of the inverse modeling show that significant displacement occurred on a shallow, elongated, north-northeast trending fault. This secondary fault slip is required to explain the north-northeast trending linear area with high range change gradient in the interferogram. What role may this secondary fault play in this earthquake sequence? Most of the early aftershocks occurred along this trend (Figure 2). This led *Ichinose et al.* [1998] to conclude that also the main shock occurred along this trend. We argue here that the observed ground deformation and seismicity in this area is associated with slip on a secondary fault conjugate to the main fault, and that this slip was triggered by the main shock.

[28] To test this hypothesis, we examine static (Coulomb) stress changes induced by the main shock. A series of studies during the past years have shown that static stress interactions between earthquakes are important in controlling the occurrence and timing of future events [e.g., *King et al.*, 1994; *Stein*, 1999; *King and Bowman*, 2003]. Earthquakes tend to occur on faults where failure has been encouraged by previous events (stress triggering) and tend to avoid faults where failure has been discouraged by

previous earthquakes (stress shadowing). Whether failure of a fault has been encouraged or discouraged is conveniently be measured in terms of the Coulomb failure stress change $\Delta\sigma_f = \Delta\tau + \mu\Delta\sigma_n$, with $\Delta\tau$ the shear stress change on the fault (positive in slip direction), $\Delta\sigma_n$ the normal stress change on the fault (positive if the fault in unclamped), and μ the coefficient of friction. An increase of shear stress and a decrease of normal stress (unclamping) encourage failure. We would expect triggered slip on faults with positive $\Delta\sigma_f$.

[29] The Coulomb failure stress change due to the DSF earthquake together with the shallow seismicity (depth 0–6 km) is shown in Figure 6. We have used the main shock dislocation parameters of model B and consider $\Delta\sigma_f$ for normal faulting on north-northwest trending faults (with geometry of the secondary dislocation of model B) at 2 km depth. It can be seen in Figure 6 that most of the north-northeast trending aftershocks (including the principal aftershock) occurred in an area where the Coulomb failure stress was increased by 0.5–1 bar, suggesting that those events may be triggered by the main shock. The secondary dislocation of model B (with geometry based on the moment tensor solution of the principal aftershock) roughly follows this seismicity and normal slip is also consistent with Coulomb failure stress changes. This supports our hypothesis of triggered slip on the north-northeast trending fault. Note that the seismicity on the south-southeast continuation of the main shock dislocation in an area of stress decrease (shown blue) is not significant because those events occurred on north-northwest trending faults but stress changes are shown for north-northeast trending faults.

[30] Most of the north-northeast trending aftershocks are small events with magnitude <4 (Figure 6). Using the catalogue of *Ichinose* [2000], we calculate a cumulative moment for the events along this trend of only $M_w5.35$ with the main share provided by the principal aftershock ($M_w5.3$). The cumulative seismic moment is significantly below the inferred geodetic moment for this dislocation ($M_w5.6$, Table 1). This suggests that most of the triggered fault slip was aseismic and that only small patches of this fault were ruptured by earthquakes.

8. Main Shock Focal Plane

[31] An important question to understand this earthquake sequence is which of the nodal planes ruptured during the main shock and which was the sense of the coseismic strike-slip component. *Ichinose et al.* [1998] suggested that the main shock was a left-normal oblique-slip event on a north-northeast trending fault. The main problem with this interpretation is that there is no surface expression of a fault that may have ruptured.

[32] The local tectonics, the location of the earthquake, and the moment tensor solution, suggest that the earthquake was a right-normal oblique-slip event on the DSF fault. The DSF fault is the only major fault in the epicentral area. The epicenter was located ~3 km southwest of the surface trace of the fault. For a fault dip of ~65° to the southwest (inferred from the focal mechanisms of the aftershocks) the hypocenter at 6 km depth locates on the fault surface. In addition, the focal mechanism of the main event is similar to the focal mechanisms of the aftershocks farther southeast on
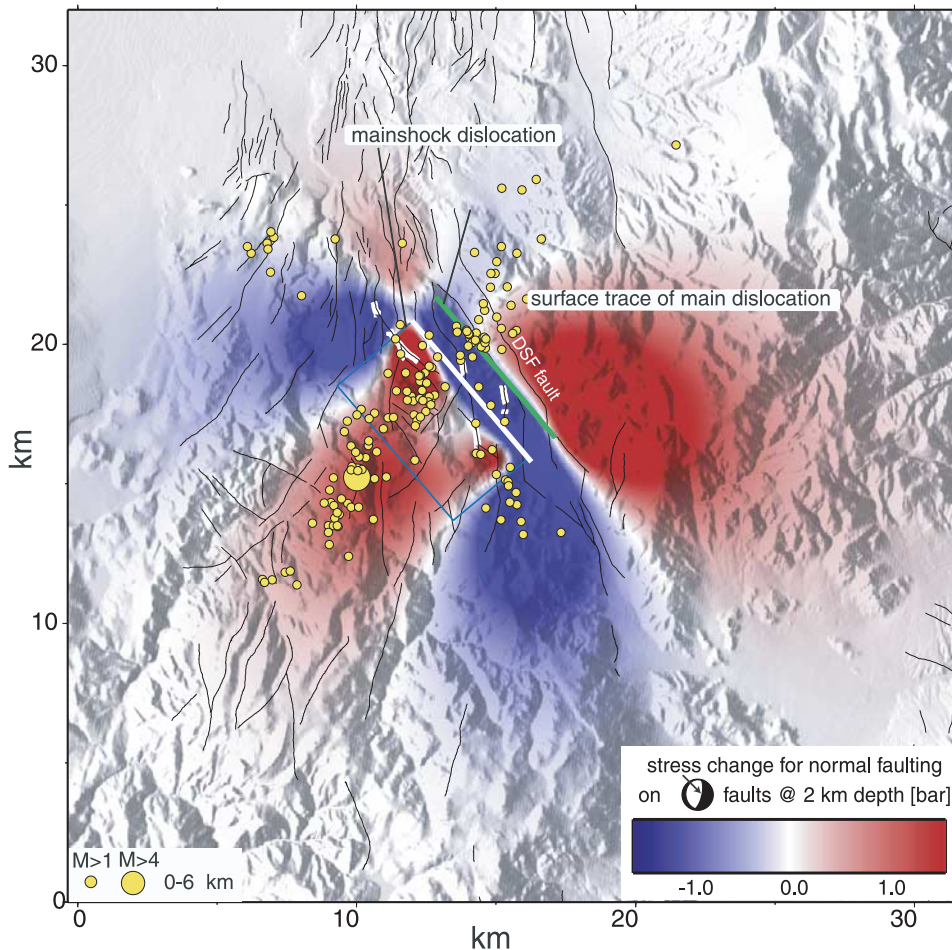
Figure 6. Coulomb stress changes due to the main shock resolved for normal faulting on N20°E, 60°E dipping fault planes at 2 km depth together with first week of shallow aftershocks (at 0–6 km depth). The north-northeast trending, normal-faulting events locate in areas of stress increase. The displayed stress change component is not relevant for the north-northwest trending, right-oblique events on the DSF fault. White line denotes the upper edge, and green line denotes the surface projection of the preferred dislocation.

the DSF fault, suggesting that the main shock and the aftershocks ruptured the same fault. In 1978 a sequence of small-magnitude ($M \geq 3.0$) events with a main shock of $M5.0$ occurred in Diamond Valley, ~10 km to the west of the DSF event. P wave first motions for the main event defined a strike-slip mechanism (Figure 1b). On the basis of the aftershock migration pattern, right-lateral faulting was assigned to a northwest striking nodal fault [*Somerville et al.*, 1980], roughly subparallel to the DSF fault.

[33] The InSAR data presented in this article provide additional arguments that the DSF earthquake occurred on the DSF fault. First, the inverse modeling of the InSAR data favors models with the main shock on the north-northwest trending nodal plane. Second, the surface projection of the InSAR-derived main shock dislocation agrees within only ~1 km with the mapped surface trace of the DSF fault (Figure 6). Third, and most importantly, the InSAR data reveal evidence for right-lateral surface displacements associated with the north-northwest trending ground cracks. We interpret these displacements as coseismic slip on surface faults splaying from the DSF fault at depth. The

left-stepping en echelon pattern of the ground cracking [*Ramelli et al.*, 1994] is also suggestive of a north-northwest trending right-lateral main fault.

[34] The main reasons for *Ichinose et al.* [1998] to conclude that the earthquake ruptured the north-northeast trending nodal plane are the first days of aftershocks that occurred along this trend. The InSAR data also require fault slip in this area. We suggest here that this fault slip is secondary and that it was triggered by the main shock. Coulomb failure stress calculations show that main shock promoted slip on this fault. Note that some of the north-northeast trending seismicity may be aftershocks of the $M_w5.3$ aftershock that occurred 12 hours after the main shock.

9. Discussion

[35] The DSF observations add to a growing body of evidence provided by spatially dense InSAR data that many earthquakes are accompanied by triggered slip on secondary faults. Triggered slip may occur along surface or concealed

faults and in the same or opposite sense as during the main shock. Examples include the 1999, Izmit earthquake [*Wright et al.*, 2001], the 1999 Hector Mine earthquake [*Fialko et al.*, 2002], the 2000 South Iceland Seismic Zone earthquake sequence [*Pedersen et al.*, 2001], and the 1998 Fandoqa, Iran, earthquake [*Berberian et al.*, 2001].

[36] The DSF observations also add to the body of evidence for conjugate faulting. Examples include the 1987 Superstition Hills, California, earthquake [*Hanks and Allen*, 1989], the 1987 M_w7.2 and M_w7.8 Gulf of Alaska earthquake sequence [*Pegler and Das*, 1996], and the 2001 M_w7.8 Wharton Basin, Indian Ocean, earthquake [*Robinson et al.*, 2001]. According to 2-D Mohr-Coulomb theory conjugate faults form at angles of $25°−30°$ from the greatest principal stress orientation [e.g., *Thatcher and Hill*, 1991]. Applying this concept to the DSF sequence (faults oriented north-northwest and north-northeast) suggest a stress state with the greatest principal stress oriented north-south and the least principal stress oriented east-west.

10. Conclusion

[37] On the basis of the InSAR data we have identified two source mechanisms for the ground deformation associated with the DSF earthquake sequence. The first source was a right-normal, oblique-slip main shock on the northwest trending DSF fault. The main shock was accompanied by coseismic ground cracking along faults subparallel to the DSF fault. The second source was shallow normal faulting on a conjugate north-northeast trending fault. This source was associated with strong aftershock seismicity during the first days following the main shock, but this seismicity accounts for only part of the InSAR-derived moment on this fault. We interpret slip on this fault as triggered seismic and aseismic slip generated by the main shock.

References

Amelung, F., D. Galloway, J. Bell, H. Zebker, and R. Laczniak, Sensing the ups and downs of Las Vegas: InSAR reveals structural control of land subsidence and aquifer-system deformation, *Geology*, 27, 483–486, 1999.

Bell, J. W., C. M. dePolo, A. R. Ramelli, A. M. Sarna-Wojcicki, and C. E. Meyer, Surface faulting and paleoseismic history of the 1932 Cedar Mountain earthquake area, west-central Nevada, and implications for modern tectonics of the Walker Lane, *Geol. Soc. Am. Bull.*, 111(6), 791–807, 1999.

Bennett, R. A., J. L. Davis, and B. P. Wernicke, Present-day pattern of Cordilleran deformation in the western United States, *Geology*, 27, 371–374, 1999.

Berberian, M., C. Baker, E. Fielding, J. A. Jackson, B. Parsons, K. Priestley, M. Qorashi, M. Talebian, R. Walker, and T. J. Wright, The 14 March 1998 Fandoqa earthquake (Mw 6.6) in Kerman province, SE Iran: Re-rupture of the 1981 Sirch earthquake fault, triggerring of slip on adjacent thrusts and the actice tectonics of the Gowk fault zone, *Geophys. J. Int.*, 146(2), 371–398, 2001.

Caskey, S. J., S. G. Wesnousky, Z. Peizhen, and D. B. Slemmons, Surface faulting of the 1954 Fairview Peak (M_s 7.2) and Dixie Valley (M_s 6.8) earthquakes, central Nevada, *Bull. Seismol. Soc. Am.*, 86, 761–787, 1996.

Cervelli, P., M. H. Murray, P. Segall, Y. Aoki, and T. Kato, Estimating source parameters from deformation data, with an application to the

March 1997 earthquake swarm off the Izu Peninsula, Japan, *J. Geophys. Res.*, 106, 11,217–11,238, 2001.

Cervelli, P., P. Segall, F. Amelung, H. Garbeil, C. Meertens, S. Owen, A. Miklius, and M. Lisowski, The 12 September 1999 Upper East Rift Zone dike intrusion at Kilauea Volcano, Hawaii, *J. Geophys. Res.*, 107(B7), 2150, doi:10.1029/2001JB000602, 2002.

dePolo, C. M., and J. G. Anderson, Estimating the slip rates of normal faults in the Great Basin, USA, *Basin Res.*, 12, 227–240, 2000.

dePolo, D. M., and C. M. dePolo, Earthquakes in Nevada 1852–1996, map, 1 sheet, Nev. Bur. of Mines and Geol., Reno, 1998.

Fialko, Y., D. Sandwell, D. Agnew, M. Simons, P. Shearer, and B. Minster, Deformation on nearby faults induced by the 1999 Hector Mine earthquake, *Science*, 297, 1858–1862, 2002.

Gianella, V. P., Earthquake and faulting, Fort Sage Mountains, California, December 1950, *Bull. Seismol. Soc. Am.*, 47, 173–177, 1957.

Hanks, T. C., and C. R. Allen, The Elmore Ranch and Superstition Hills earthquakes of 24 November 1987, *Bull. Seismol. Soc. Am.*, 79, 231–238, 1989.

Hanssen, R. F., *Radar Interferometry: Data Interpretation and Error Analysis*, 308 pp., Kluwer Acad., Norwell, Mass., 2001.

Hodgkinson, K. M., R. S. Stein, and G. Marshall, Geometry of the 1954 Fairview Peak-Dixie Valley earthquake sequence from a joint inversion of leveling and triangulation data, *J. Geophys. Res.*, 101, 25,437–25,458, 1996.

Ichinose, G. A., Seismicity and stress transfer studies in eastern California and Nevada: Implications for earthquake sources and tectonics, Ph.D. thesis, Univ. of Nev., Reno, 2000.

Ichinose, G. A., K. D. Smith, and J. G. Anderson, Moment tensor solutions of the 1994 to 1996 Double Spring Flat, Nevada, earthquake sequence and implications for local tectonic models, *Bull. Seismol. Soc. Am.*, 88, 1363–1378, 1998.

Jonsson, S., Modeling volcano and earthquake deformation from satellite radar interferometric observations, Ph.D. thesis, Stanford Univ., Stanford, Calif., 2002.

Jonsson, S., H. A. Zebker, P. Segall, and F. Amelung, Slip distribution of the 1999 M7.1 Hector Mine earthquake determined from geodetic data, *Bull. Seismol. Soc. Am.*, 92, 1377–1389, 2002.

King, G. C. P., and D. D. Bowman, The evolution of regional seismicity between large earthquakes, *J. Geophys. Res.*, 108(B2), 2096, doi:10.1029/2001JB000783, 2003.

King, G. C. P., R. S. Stein, J. Lin, and C. A. Langston, Static stress changes and the triggering of earthquakes: The 1992 Landers, California, earthquake sequence, *Bull. Seismol. Soc. Am.*, 84, 935–953, 1994.

Okada, Y., Internal deformation due to shear and tensile faults in a half-space, *Bull. Seismol. Soc. Am*, 82, 1018–1040, 1992.

Oldow, J. S., C. L. V. Aiken, J. L. Hare, J. F. Ferguson, and R. F. Hardyman, Active displacement transfer and differential block motion within the central Walker Lane, western Great Basin, *Geology*, 29, 19–22, 2001.

Pedersen, R., F. Sigmundsson, K. L. Feigl, and T. Arnadottir, Coseismic inferferograms of two M_s = 6.6 earthquakes in the south Iceland seismic zone, June 2000, *Geophys. Res. Lett.*, 28(17), 3341–3344, 2001.

Pegler, G., and S. Das, The 1987–1992 Gulf of Alaska earthquakes, *Tectonophysics*, 257(2−4), 111–136, 1996.

Ramelli, A. R., et al., Secondary surface fracturing associated with the Double Spring Flat earthquake of September 12, 1994, paper presented at Fall Meeting, AGU, San Francisco, Calif., 1994.

Ramelli, A. R., J. W. Bell, C. M. dePolo, and J. C. Yount, Large-magnitude, late Holocene earthquakes on the Genoa Fault, west-central Nevada and eastern California, *Bull. Seismol. Soc. Am.*, 89, 1458–1472, 1999.

Robinson, D. P., C. Henry, S. Das, and J. H. Woodhouse, Simultaneous rupture along two conjugate planes of the Wharton Basin earthquake, *Science*, 292, 1145–1148, 2001.

Somerville, M. R., W. A. Peppin, and J. D. VanWormer, An earthquake sequence in the Sierra Nevada-Great Basin boundary zone: Diamond Valley, *Bull. Seismol. Soc. Am.*, 70, 1547–1555, 1980.

Stein, R. S., The role of stress transfer in earthquake occurrence, *Nature*, 402, 605–609, 1999.

Stewart, J. H., Tectonics of the Walker Lane Belt, western Great Basin; Mesozoic and Cenozoic deformation in a zone of shear metamorphism and crustal evolution of the western United States, *Rubey Volume 7*, pp. 683–713, Prentice-Hall, Old Tappan, N. J., 1988.

Svarc, J. L., J. C. Savage, W. H. Prescott, and A. R. Ramelli, Strain accumulation and rotation in western Nevada, 1993–2000, *J. Geophys. Res.*, 107(B5), 2090, doi:10.1029/2001JB000579, 2002.

Thatcher, W., and D. P. Hill, Fault orientations in extensional and conjugate strike-slip environments and their implications, *Geology*, 19, 1116–1120, 1991.

Thatcher, W., G. R. Foulger, B. R. Julian, J. Svarc, E. Quilty, and G. W. Bawden, Present-day deformation across the Basin and Range Province, western United States, *Science*, 283, 1714–1718, 1999.

Wernicke, B., A. M. Friedrich, N. A. Niemi, R. A. Bennett, and J. L. Davis, Dynamics of plate boundary fault systems from Basin and Range Geodetic Network (BARGEN) and geological data, *GSA Today*, *10*(11), 1–7, 2000.

Wesnousky, S. G., and C. H. Jones, Oblique slip, slip partitioning, spatial and temporal changes in the regional stress field, and the relative strength of active faults in the Basin and Range, western United States, *Geology*, *22*, 1031–1034, 1994.

Williams, S., Y. Bock, and P. Fang, Integrated satellite interferometry: Tropospheric noise, GPS estimates, and implications for interferometric synthetic aperture radar products, *J. Geophys. Res.*, *103*, 27,051–27,068, 1998.

Wright, T., E. Fielding, and B. Parsons, Triggered slip; observations of the 17 August 1999 Izmit (Turkey) earthquake using radar interferometry, *Geophys. Res. Lett.*, *28*(6), 1079–1082, 2001.

Zoback, M. L., State of stress and modern deformation of the northern Basin and Range province, *J. Geophys. Res.*, *94*, 7105–7128, 1989.

———————————

F. Amelung, Division of Marine Geology and Geophysics, Rosenstiel School of Marine and Atmospheric Sciences, 4600 Rickenbacker Causeway, Miami, FL 33149, USA. (amelung@rsmas.miami.edu)

J. W. Bell, Nevada Bureau of Mines and Geology, University of Nevada, Reno, NV 89557, USA. (jbell@unr.edu)